Kent Academic Repository

Full text document (pdf)

Citation for published version

DOI

Link to record in KAR

Document Version

Author's Accepted Manuscript

Influence of Surfactant Structure on Photoluminescent π-Conjugated Polymer Nanoparticles: Interfacial Properties and Protein Binding

Laura Urbano[a], Luke Clifton[c], Hoi Ki Ku[a], Hannah Kendall-Troughton[a], Kalliopi-Kelli A. Vandera[a], Bruno F.E. Matarese[g], Thais Abelha[a], Peixun Li[c], Tejal Desai[b], Cécile A. Dreiss[a], Robert D. Barker[d], Mark A. Green[e], Lea Ann Dailey*[f], Richard D. Harvey[f]

KEYWORDS

Conjugated polymer nanoparticles, protein corona, PEG, surfactants, albumin binding

ABSTRACT

Π-conjugated polymer nanoparticles (CPNs) are under investigation as photoluminescent agents for diagnostics and bioimaging. To determine whether the choice of surfactant can improve CPN properties and prevent protein adsorption, five non-ionic polyethylene glycol alkyl ether surfactants were used to produce CPNs from three representative π-conjugated polymers. The surfactant structure did not influence size or yield, which were dependent on the nature of the

conjugated polymer. Hydrophobic interaction chromatography, contact angle, quartz crystal microbalance and neutron reflectivity studies were used to assess the affinity of the surfactant to the conjugated polymer surface, and indicated that all surfactants were displaced by the addition of a model serum protein. In summary, CPN preparation methods which rely on surface coating of a conjugated polymer core with amphiphilic surfactants may produce systems with good yields and colloidal stability *in vitro*, but may be susceptible to significant surface alterations in physiological fluids.

INTRODUCTION

Conjugated polymer nanoparticles (CPNs) show promise as highly biocompatible optical imaging systems, and have been the object of exploration for numerous biological applications[1–6]. The preparation conditions can influence several parameters, including particle size, particle size distribution, percentage product yield, colloidal stability, and optical properties[6–8]. Therefore, the choice of production method and stabilizing excipients used is central to performance optimization and industrial scale-up of CPNs. One of the major shortcomings in this rapidly expanding field is the lack of published information regarding the impact of post-synthetic CPN fabrication techniques on the final product. Much of the information on this topic is dispersed in the literature and restricted to very specific polymers/formulations. Information, such as nanoparticle yield values and optical stability, and the rationale behind the choice of production conditions are rarely reported. When such values are published, they reveal major shortcomings, or at best a great variability in current preparation techniques for CPNs[9,10].

Another important issue insufficiently addressed in the literature is the stability of CPNs in biological media. Currently, many studies investigating CPNs for bioimaging purposes utilize core-shell nanoparticle systems, comprised of a conjugated polymer core surrounded by a shell of adsorbed surfactant molecules that promotes colloidal stability of the particles, and is occasionally further functionalized with a targeting moiety[11–13,9]. However, surface coatings which rely on hydrophobic interactions between the conjugated polymer and the surfactant, can be destabilized in biological fluids. Plasma proteins can easily displace a proportion of the surfactant from the particle surface forming a protein corona[14,15], thus compromising CPN functionality when introduced into a biological environment. Hence, it is important to study the

interactions of surfactant chemistries used to coat CPN surfaces, to determine whether the stability of the coating layer can be enhanced in the presence of biological fluids.

The aim of this study was to perform a systematic investigation to determine whether surfactant structure can influence CPN properties and protein binding using three representative conjugated polymers: F8BT, CN-PPV and PCPDTBT. The polymers were chosen either due to their high quantum yield values (F8BT, CN-PPV) or their broad absorption/emission spectra (PCPDTBT)[16–19]. Instead of comparing the widely disparate surfactant structures reported in the literature, a series of high purity polyethylene glycol alkyl ether (CxEy) surfactants were chosen as model surfactants to systematically investigate the impact of i) the lipophilic component of the surfactant (alkyl chain length: C_{12}-C_{18}), ii) the hydrophilic component (PEG chain length: E_{6}-E_{100}) and/or iii) the overall hydrophilic:lipophilic ratio (hydrophilic-lipophilic balance, HLB, values: 11.7-18.0) on the CPN properties (Figure 1). CPNs were produced according to a modified nanoprecipitation method[20] using 1 mM surfactant. The resulting percentage product yield, particle size distribution, optical properties and protein binding of the systems were evaluated. Zeta potential, hydrodynamic interaction chromatography (HIC), contact angle measurements, quartz crystal microbalance with dissipation (QCM-D), and neutron reflectivity were employed to study the adsorption behaviour and the formation of different interfacial structures of both surfactant and bovine serum albumin (BSA) on the surface of the CPNs. BSA was chosen as a model protein, because of its abundance in serum and its ability to interact with amphiphilic compounds of various nature[21–25]. Accordingly, it was likely to interact easily with the PEGylated surfactants, competing with them to bind the hydrophobic conjugated polymer forming the nanoparticle core. It was expected that surfactants with higher lipophilicity (i.e. lower HLB value) would show a higher affinity to the hydrophobic conjugated polymer core of

the respective CPN systems, thus resulting in smaller nanoparticle sizes, higher percentage yield

values, increases in optical brightness and stability, as well as stability against displacement by

proteins.

Figure 1. Structure and selected properties of a) the conjugated polymers forming the CPN core

(F8BT, CN-PPV and PCPDTBT) and b) the CxEy surfactants used to coat the CPN core. C) A

schematic of the core/shell structure of CPNs.

EXPERIMENTAL SECTION

MATERIALS - Conjugated polymers, poly(2.5-di(hexyloxy)cyanoterephthalylidene) (CN-

PPV, average molecular weight (Mw): 40,000-70,000 and poly[(9,9-di-n-octylfluorenyl-2,7-

diyl)-*alt*-(benzo[2,1,3]thiadiazol-4,8-diyl)] (F8BT, average Mw: 10,000-20,000 g mol^{-1},

polydispersity$\leqq$ 3.00) Reagents poly[2,6-(4,4-bis-(2-ethylhexyl)-4H-cyclopenta [2,1-b;3,4-b dithiophene)-alt-4,7(2,1,3-benzothiadiazole)] (PCPDTBT; Mw: 7,000-20,000 g mol^{-1}) were purchased from Sigma-Aldrich (UK). Polyoxyethylene (23) lauryl ether (Brij® S100, $C_{12}E_{100}$, Mw: 1,198 g mol^{-1}, Brij® L23 solution, $C_{12}E_{23}$, 30% (W/V) in H_2O, Mw: 1,198 g mol^{-1}, HLB 16.9), polyoxyethylene (20) stearyl ether (Brij® S20, $C_{18}E_{20}$, Mw: 1,150 g mol^{-1}, HLB 15.3) and polyoxyethylene (10) oleyl ether (Brij® O10, $C_{18-1}E_{10}$, Mw: 709 g mol^{-1}, HLB 12.4), hexaethylene glycol monododecyl ether ($C_{12}E_6$, HLB 11.6, Mw: 450.65 g mol^{-1}), albumin from bovine serum (fraction V, essentially protease free, $\geq$92% (GE)) and tetrahydrofuran (THF RegentPlus®, $\geq$99+%) were purchased from Sigma-Aldrich Corporation (UK). The $d_{25}C_{12}E_6$ and $C_{18}E_{20}$ surfactants used for neutron reflectometry studies, were custom synthesized by the ISIS Deuteration Facility at the Rutherford Appleton Laboratory (Science and Technology Facilities Council, UK).

Surfactant characterisation

The adsorption of surfactants at the air-water surface was assessed by measuring the surface pressure. A Langmuir trough (NIMA Technologies Ltd., Coventry, UK) equipped with a calibrated NIMA PS4 pressure sensor and a Wilhelmy plate (Whatman, grade 1, chromatographic paper), connected to a controlling computer with the NIMA IU4 interface unit software was used. For all the experiments a PFA petri dish (Chemware®, Chemfluor® PFA, Petri Dish, Saint-Gobain Performance Plastics, D1069544, Batch # G664) with diameter 50 mm, height 10 mm and volume capacity 20 mL was placed over a magnetic stirring plate on the PTFE Langmuir trough top surface. A subphase free from dust and contaminants (ultra-pure water, 18.2 MΩ·cm) was poured into the petri dish and a clean Wilhelmy plate was suspended from the meter arm of the Langmuir trough and submerged into the subphase. Each surfactant solution

was injected (100 mL of 1 mg mL^{-1}) in the subphase while stirring. The adsorption of the drug on the surface causes changes in surface pressure which are recorded over time under a constant surface area (21.3 A^2 m^{-1}) at 23°C. Each sample was run in triplicate (n=3) and the changes in surface pressure were plotted against time (P&A-Time isotherm). The P-Time isotherm was fitted with a sigmoidal model (Hill plot with 3 parameters) using SigmaPlot 13.0 software in order to analyse the kinetics of the process. The model is described by

Equation 1: $f(x) = \frac{\Pi * x^b}{t50\%^b + x^b}$

where Π is the maximum surface pressure reached at the plateau, b is the Hill coefficient of sigmoidicity (hill slope at its midpoint) and $t50\%$ is the time for which 50% of maximum pressure is obtained.

CPN production

Nanoparticles were produced via a modified nanoprecipitation method. Stock solutions of F8BT, CN-PPV and PCPDTBT (1.5 mg mL^{-1}) were prepared in THF. Aqueous surfactant dispersions ($C_{12}E_{100}$, $C_{12}E_{23}$, $C_{18}E_{20}$, $C_{18\text{-}1}E_{10}$, $C_{12}E_6$; 1mM, 30 mL) were prepared and stirred for 10 minutes prior to use. The polymer stock solution (1 mL) was added dropwise to the surfactant dispersion whilst stirring, sonicated in an ultrasonic bath at 44Hz for 90 seconds (XUBA3 Ultrasonic bath Grant, UK) remove incompletely formed and unstable aggregates, and to facilitate evaporation of organic solvent present in nanosuspension[26]. Suspensions were further stirred overnight for complete evaporation of the THF. Volumes were re-adjusted to 30 mL with distilled water prior to use and CPN suspensions were stored at 4°C.

Dynamic light scattering

The average hydrodynamic diameter was measured (n=3 replicates) by dynamic light scattering (DLS) using a Zetasizer Nano ZS (Malvern Instruments Ltd, Worcestershire, UK).

Size was measured at 25 °C, with backscatter detection at a measurement angle of 173° and a

refractive index of 1.59.

Percentage yield

The percentage yield was defined as the percentage of nanoparticles within a given batch with

a Stokes diameter < 500 nm. The threshold was chosen based on the extended definition of

nanoparticle size (limit 500 nm[27]). The Stokes diameter was chosen as an equivalent measure of

particle size, due to the ease of separating particles of different sizes based on sedimentation

velocity during centrifugation (see Supplementary Information for further details). Aliquots of

nanosuspension (1 mL; n=3 replicates for each formulation) were centrifuged at 5111g for 10

minutes (Heraeus™ Pico™ Microcentrifuge, Thermo Fisher Scientific, USA). The pellet and

supernatant were separated, and all samples were dried. THF (1mL) was added to each sample

and the concentration of conjugated polymer was determined using UV spectrophotometry

(Lamba 2S, Perkin Elmer Inc., USA). The percentage yield of nanoparticles with a Stoke's

diameter < 500 nm (i.e. supernatant fraction) was calculated according to Equation 2:

Equation 2: $Percentage\ yield\ of\ nanoparticles = \frac{[Supernatant]}{[Supernatant]+[pellet]} \times 100\%$

Photoluminescence and quantum yield

The photoluminescence of F8BT and CN-PPV CPN formulations (n=3 replicates) in water was

measured with a luminescence spectrometer (LS50B, PerkinElmer Ltd). F8BT and CN-PPV

were excited at 470 and 430 nm, respectively, and an emission scan was recorded from 500-800

nm (ex/em slits 4 nm/4 nm). The photoluminescence of PCPDTBT CPN formulations (n=3

replicates) in water was measured using a spectrofluorometer (Fluoromax-4, Horiba). PCPDTBT

CPNs were excited at 410, and an emission scan was recorded from 450-800 nm (ex/em slits 5

nm/5 nm). The photoluminescence quantum yields (PLQYs) were measured using an absolute

PLQY spectrometer (C11347 Quantaurus-QY, Hamamatsu Photonics, Japan).

Hydrophobic interaction chromatography

Hydrophobic interaction chromatography[28] was used to characterize surfactant affinity to the

conjugated polymer core, as well as protein adsorption to the particle surface using bovine serum

albumin (BSA) as a model protein. CPN suspensions (n = 3 individual batches) were prepared as

described above with either $C_{12}E_6$ or $C_{18}E_{20}$, and diluted to a concentration of 50 μg mL^{-1} in

distilled water with or without 1 mg mL^{-1} BSA then incubated for 1 hour at 37 °C. Non-particle

bound BSA and excess surfactant were removed by centrifugation, removal of the supernatant

and resuspension in PBS. The washing procedure was repeated twice. Suspensions (250 μL)

were then eluted with PBS through three different HiTrap™ substituted sepharose hydrophobic

interaction columns: butyl FF, phenyl FF (high substitution) and octyl FF (GE Healthcare Life

Sciences, Little Chalfont, UK). The eluent was collected in 8 fractions (1 mL) and analysed for

particle content via UV absorbance (SpectraMax 190, Molecular Devices, CA, USA; λ = 450

nm) [29]. Particles retained in the column were subsequently eluted using 1% Triton X-100,

whereby the eluent was collected in a further 8 fractions (1 mL). Absorbance values were plotted

against elution volumes and two area under the curve (AUC) values were calculated using

Prism™ 6.0 software (Graphpad Prism 5, CA, USA). The particle retention (%R) in each of the

three columns was defined according to **Equation 3:**
$$\%R = \left(\frac{\text{AUC TritonX}}{\text{AUC PBS} + \text{AUC TritonX}} \right) \times 100$$

The HIC index value was calculated according to

Equation 4:
$$\text{HIC index} = \frac{\left(\%R_{\text{butyl}} \times 0.47\right) + \left(\%R_{\text{phenyl}} \times 0.94\right) + \left(\%R_{\text{octyl}} \times 2.05\right)}{\left(100\% \times 0.47\right) + \left(100\% \times 0.94\right) + \left(100\% \times 2.05\right)}$$

Whereby, 0.47, 0.94 and 2.05 represent the logP values of each column linker (butyl, phenyl and octyl modified columns, respectively) as calculated using Marvin Sketch (version 5.5.0.1, Chem Axon Limited). In the denominator, each logP value was multiplied by 100%, which represents the theoretical case of 100% retention on each column achieved by a particle with maximum hydrophobicity. HIC index values of 1.0 indicate maximum hydrophobicity and 0.0 minimum hydrophobicity[14].

Zeta potential

CPN suspensions were prepared as described above with either $C_{12}E_6$ or $C_{18}E_{20}$, diluted to a concentration of 50 µg mL^{-1} in distilled water, with or without 1 mg/mL BSA, and incubated for 1 h at 37 °C. Non-particle bound BSA and excess surfactant were removed by centrifugation, removal of the supernatant and resuspension in 5 mM NaCl. The washing procedure was repeated two times. The zeta potential was measured (n=3 individual batches) using the Nanosizer in 5 mM NaCl at 25 °C and Zetasizer Software 6.20 was used to analyse the data.

Contact angle measurements

Solutions of F8BT (2 mg/mL in chloroform), CN-PPV (2 mg/mL in chloroform), and PCPDTBT (2 mg mL^{-1} in THF) were prepared for spin-coating of thin polymer films onto silicon wafers. Spin coating was performed by flooding the wafer surface with polymer solution and rotating under a nitrogen atmosphere at 4500 rpm (acc. 1500) for 30 s using a Süss MicroTec spin coater (Delta 6 RC TT, Süss MicroTec Lithography GmbH, Germany). The sessile droplet method was used to measure the contact angle of six 10 µL droplets of purified water (18.2 MΩ) applied randomly across a single thin film surface. The measures were performed over a total of 6 thin films (two for each polymer) using a DP-M17 USB Digital Microscope (Conrad

Electronics, UK). Three films were subsequently submerged in 10 mL surfactant solution (1 mM $C_{18}E_{20}$, and $C_{12}E_6$, respectively) and incubated at ambient room temperature for 15 minutes, followed by gentle rinsing with purified water (5x) and drying under nitrogen prior to contact angle measurements of six further 10 µL droplets of purified water. Surfactant-treated films were then submerged in 10 mL BSA solution (1 mg mL^{-1}) and incubated at ambient room temperature for 15 minutes, followed by gentle rinsing with purified water (5x) and drying under nitrogen prior to contact angle measurements of six further 10 µL droplets of purified water. The contact angle was measured based on image analysis, using ImageJ software with the plug-in Drop Shape Analysis based on B-spline snakes algorithm[30]. Contact angle measurements were reported as the mean ± standard deviation of n=6 droplets per film.

Quartz crystal microbalance

Conjugated polymer thin films were prepared by spin-coating onto gold-coated quartz crystals (Q-Sense, Biolin Scientific, Stockholm, Sweden). Spin coating was performed as described above. Quartz crystal microbalance with dissipation monitoring (QCM-D) experiments[31] were conducted on a Q-Sense E4 instrument (Q-Sense, Sweden). After stabilization of the baseline in deuterated water, changes in resonant frequency Δf and energy dissipation ΔD were monitored as a function of time using overtones 3 to 13 (15 to 65 MHz). Surfactant solution (d $C_{12}E_6$ or d $C_{18}E_{20}$, 1 mM) was continuously injected in the chamber for 10 mins then allowed to adsorb for 5 min. The chamber was then rinsed with D_2O continuously injected for 10 mins and then allowed to rest for 5 min ensuring enough time for the F and D to stabilize. BSA solution 1 mg mL^{-1} was then injected over for 10 mins then allowed to adsorb for 5 min. The chamber was then rinsed with D_2O continuously injected for 10 mins and then allowed to rest for 5 min ensuring enough time for the F and D to stabilize Q-Tools software (Q-Sense AB, Gothenburg,

Sweden) was used to analyse the QCM data. For each condition, the experiments were repeated 3 times. The measurements were found to be reproducible and a representative data set are presented.

Neutron reflectometry

Specular neutron reflectometry (NR) measurements were carried out using the white beam INTER reflectometer[32] at the Rutherford Appleton Laboratory (Oxfordshire, UK), employing neutron wavelengths from 1.5 to 16 Å. The reflected intensity was measured at two glancing angles, being 0.7° and 2.3°, as a function of the momentum transfer, Qz (Qz = $(4\pi \sin \theta)/\lambda$ where λ is wavelength and θ is the incident angle). This yielded data over a Qz range of ~0.01 to 0.3 Å-1 with a resolution (dQ/Q) of 3.5% and a total illuminated length of 60 mm.

The samples were prepared by spin-coating F8BT polymer onto the polished surfaces of cleaned 50 × 100 × 10 mm silicon substrates (Crystran Ltd, Poole, UK). The surface of each substrate was flooded with a 0.2% w/v solution of F8BT in chloroform and spun at 3000 rpm for 30 s under vacuum. The resultant coated substrates were then secured into flow cells purpose built for analysis of silicon-liquid interfaces, which were placed on a variable-angle sample stage in the NR instrument. The inlets to the flow cells were connected to a liquid chromatography pump (L7100 HPLC pump, Merck, Hitachi) which allowed for easy exchange of the solution isotopic contrast within each (3 mL volume) solid-liquid sample cell.

Three F8BT-coated silicon substrates were prepared, which were all characterised by NR in three different solvent contrasts; D_2O, H_2O and silicon-matched water (SMW, a mixture of 62% H_2O and 38% D_2O). One sample was exposed (via the HPCL pump) to a 1 mg mL^{-1} solution of BSA in D_2O and incubated for 1 hour, prior to flushing of the excess BSA and NR measurement. The further two samples were first exposed to 1 mM surfactant solutions (either $d_{25}C_{12}E_6$ or

$C_{18}C_{20}$) in H_2O and incubated for 1 hour, prior to flushing of the excess surfactant and NR measurement. The surfactant-coated F8BT samples were subsequently incubated with BSA (1 h) before flushing of the excess protein and final NR measurements. After the initial characterisation of the polymer films, four solvent contrasts were used; D_2O, H_2O, SMW and polymer-matched water (PMW, a mixture of 76% H_2O and 24% D_2O with a scattering length density of 1.106×10^{-6} Å^{-2}, based on an estimated SLD for F8BT). All measurements were carried out at ambient temperature (298 K).

The NR data were analysed using the in-house software, RasCal (A. Hughes, ISIS Spallation Neutron Source, Rutherford Appleton Laboratory) which employs an optical matrix formalism (described in detail by Born and Wolf[33]) to fit Abeles layer models to the interfacial structure. In this approach the interface is described as a series of slabs, each of which is characterised by its scattering length density (SLD), thickness and roughness, where the roughness parameter is applied as a Gaussian smearing across the interface. The reflectivity for the model starting point is then calculated and compared with the experimental data. A least squares minimisation is used to adjust the fit parameters to reduce the differences between the model reflectivity and the data. In all cases the simplest possible model (i.e. least number of layers), which adequately described the data, was selected.

Statistics

Statistical analyses were conducted using Graph Pad Prism (San Diego, CA). $p < 0.05$ were considered significant: * <0.05, ** <0.01, *** <0.001.

Results and Discussion

Effect of surfactant structure on CPN properties

Prior to their use in nanoparticle preparation, the five C_xE_y surfactants chosen for study (HLB: 11-18) were characterised with regard to their adsorption behaviour at the air-water interface using a Langmuir trough (Figure 2). The surface pressure-time isotherms depicted in Figure 2 describe the dynamic formation of a surfactant monolayer at the air-liquid interface and can be used as a first approximation to surfactant adsorption processes from the aqueous phase onto the hydrophobic conjugated polymer surface during CPN formation. As hypothesized, a rough correlation between surfactant HLB value and accumulation at the interface was observed, whereby the more hydrophobic surfactants (lower HLB values) generally showed a higher surface pressure compared to hydrophilic surfactants (higher HLB values) and thus could be predicted to show a higher affinity to a hydrophobic polymer surface. However, it was also observed that C_{12} surfactants exhibited a multi-step adsorption isotherm, which indicated that multiple adsorption or desorption processes occurred prior to reaching a maximum equilibrium state. In contrast, C_{18} surfactants organised themselves rapidly at the air-water interface resulting in a single step adsorption isotherm. The isotherms of all the surfactants, apart from the $C_{12}E_6$, exhibited a good fit to the Hill equation with three parameters (Table 2). For $C_{12}E_6$, the Hill equation could only be used to characterise the first adsorption equilibrium event.
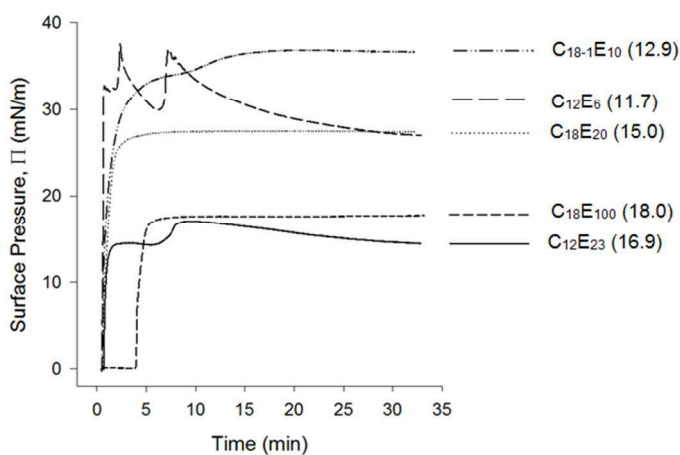
Figure 2. Surface pressure-time isotherms on a distilled water sub-phase after injection of five different non-ionic surfactant solutions. The adsorption studies were conducted under constant area (21.3 A^2) and temperature (23 °C) with curves representative of n=3 experiments.

Table 2: Coefficients from the Hill equation used to fit the pressure-time isotherms. Π is the maximum surface pressure reached, $t_{1/2}$ the time needed to reach 50% of Π and ($\Pi/2$) is the half maximum surface pressure. These data are presented as mean ± std (n=3).

Theoretical model: $f(x) = \dfrac{\Pi * x^b}{t_{50\%}{}^b + x^b}$					
Sample	1st Π (mN m^{-1})	Hill coefficient (b)	$t_{50\%}$(min)	1st $\Pi/2$ (mN m^{-1})	Surface equilibrium pressure (mN m^{-1})
C$_{12}$E$_6$	34.42 ± 1.30	-	0.65 ± 0.04	17.90 ± 1.70	27.96 ± 0.60
C$_{18-1}$E$_{10}$	36.36 ± 0.40	1.94± 0.50	1.21 ± 0.33	18.67 ± 1.10	36.14 ± 0.60
C$_{18}$E$_{20}$	27.93 ± 0.50	2.44 ± 0.90	1.18 ± 0.02	14.72 ± 0.40	27.96 ± 0.60
C$_{18}$E$_{100}$	16.81 ± 0.60	6.77 ± 3.30	0.62 ± 0.05	10.82 ± 0.40	17.16 ± 1.10
C$_{12}$E$_{23}$	15.34 ± 1.20	-	0.66 ± 0.01	9.50 ± 1.00	15.12 ± 1.00

CPNs were produced with a modified nanoprecipitation method using the five different C$_x$E$_y$ surfactants as surface stabilisers and exhibited different particle size and yield values (Figure 3). It was observed that conjugated polymer properties, as opposed to the nature of the surfactant, were more influential in determining CPN size and yield, with all F8BT (214-296 nm) nanoparticles significantly larger (P<0.05 and P<0.1; two-way ANOVA test with Bonferroni post-test) than their CN-PPV (106-135 nm) and PCPDTBT (122-146 nm) counterparts. The

polydispersity values of all CPNs (Table 2) show that CN-PPV nanoparticles were more narrowly dispersed than the F8BT and PCPDTBT systems.

The hydrodynamic diameters observed in this study were larger than those reported for CPNs prepared by nanoprecipitation, especially the so-called polymer dots (Pdots[4]). This is likely due to the higher concentration of conjugated polymer in THF (1500 vs. 20 ppm[4]) used in the current study. The rationale for increasing the conjugated polymer concentration in the organic phase resulted from a general need to produce more highly concentrated CPN suspensions for cell-based assays, such as cytotoxicity tests[9,15]. Such assays require highly concentrated CPN dispersions to generate dose-response curves over an appropriately broad concentration range [9,15]. Electron micrographs of selected samples from previous studies suggest that the size distribution of the predominantly spherical particles is multimodal, with a majority of the CPN in the 20-50 nm size range and a significant fraction of larger particles >100 nm[16]. As the intensity-weighted Z-average values of the CPN are depicted in Figure 2, the calculated average particle sizes are likely to be weighted towards larger hydrodynamic diameters.

F8BT CPN exhibited consistently larger hydrodynamic diameters compared to CN-PPV and PCPDTBT nanoparticles. This may be due to a combination of factors influencing the nanoprecipitation process, including CP concentration and solubility in THF, surface tension and viscosity of the organic phase, as well as THF diffusivity in water. A recent study by Huang and Zhang (2018) report that water-miscible organic solvents with a comparatively low diffusion coefficient in water, such as THF, produce larger, more polydisperse nanoparticles compared to solvents with higher diffusion coefficients[34]. Additionally, the solubility of the conjugated polymer in THF might also play an important role. Polymer solubility in solvents can be estimated by the difference in Hildebrand solubility parameter values, with similar values

indicating a good solubility[35]. The reported Hildebrand solubility parameter for F8BT (18.6-19.0 MPa$^{1/2}$)[35] is much closer to THF (18.5 MPa$^{1/2}$) [ref] than that of, e.g. PCPDTBT (21.8 MPa$^{1/2}$)[36]. Thus, it may be speculated that a higher amount of soluble F8BT enriches in the THF phase during the comparatively slow solvent diffusion process, leading to larger polymer aggregates during precipitation, as well as higher overall polydispersity values.
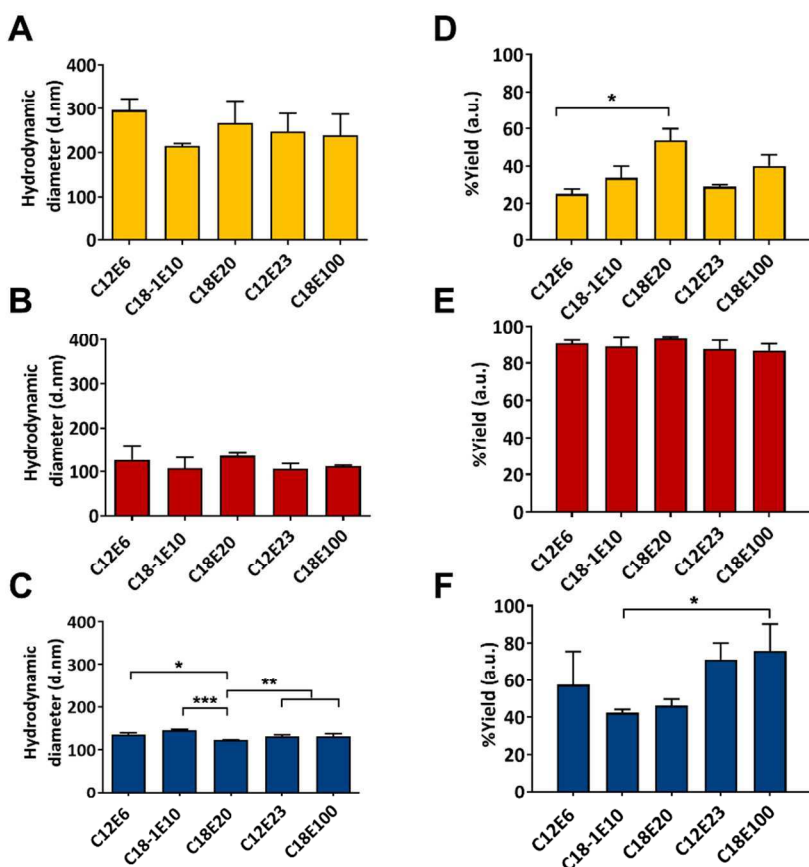
Figure 3. Particle size and percentage yield of (A,D) F8BT, (B,E) CN-PPV and (C, PCPDTBT nanoparticles. Values represent the mean ± standard deviation of n=3 CPN batches *p < 0.05, **p < 0.01, ***p < 0.001.

Table 3. Polydispersity index values of F8BT, CN-PPV and PCPDTBT nanoparticle size distribution profiles. Values represent the mean ± standard deviation of n=3 CPN batches.

Surfactant	HLB	Polydispersity index		
		F8BT	CN-PPV	PCPDTBT
$C_{18}E_{100}$	18.0	0.36 ± 0.09	0.09 ± 0.07	0.10±0.01
$C_{12}E_{23}$	16.9	0.26 ± 0.10	0.14 ± 0.10	0.11±0.01
$C_{18}E_{20}$	15.0	0.37 ± 0.08	0.08 ± 0.03	0.10±0.01
$C_{18-1}E_{10}$	12.9	0.21 ± 0.03	0.11 ± 0.05	0.09±0.01
$C_{12}E_6$	11.7	0.36 ± 0.02	0.09 ± 0.02	0.09±0.01

All CN-PPV nanoparticles were prepared with very high yields (span 87-93%), which were significantly ($P<0.001$) higher than F8BT and PCPDTBT yields (~20-60%) (Figure 3). The yield values for F8BT nanoparticles were consistent with results reported by Khanbeigi et al (2015), who observed similar yields (~20-40%) when manufacturing F8BT CPNs coated with Solutol® HS 15 or sodium dodecyl sulfate[14]. Interestingly, yield results differed considerably within the F8BT and PCPDTBT nanoparticle groups, although no relationship between surfactant HLB value and nanoparticle yield was observed. Instead, it appeared that the use of C_{12} surfactants typically resulted in lower yield values compared with C_{18} surfactants. This effect may be related to the tendency of C_{12} surfactants to undergo multiple adsorption/desorption processes (Figure 2) prior to reaching adsorption equilibrium at an interface, which suggests that the surface stabilising effect of C_xE_y surfactants may be enhanced by increasing the length of the alkyl chain, rather than by decreasing the overall HLB value.

Photoluminescence emission profiles were also dictated primarily by the conjugated polymer properties, rather than the surfactant structure (Figure 4). For example, the highly planar

conformation of F8BT is responsible for its high singlet fraction and therefore bright photoluminescence [37–40], with quantum yield values of 41-42%. In contrast, the coiled conformation of CN-PPV has been reported to make it susceptible to auto-quenching, [41–44] which was also observed in the current study, where CN-PPV systems had a quantum yield value of 34-35%. PCPDTBT, which is excited and emits in the near-infrared range, is reported to have low quantum yield values of 0.1%[45], which were also confirmed in this study (1%). The choice of surfactant did not influence the emission profiles of the CPNs, which showed stable emission spectra in deionized water with a peak around 630 nm for CN-PPV and 536 nm for F8BT. Furthermore, incubation with BSA did not produce any significant change in terms of absolute quantum efficiency (See Figure 4 b).
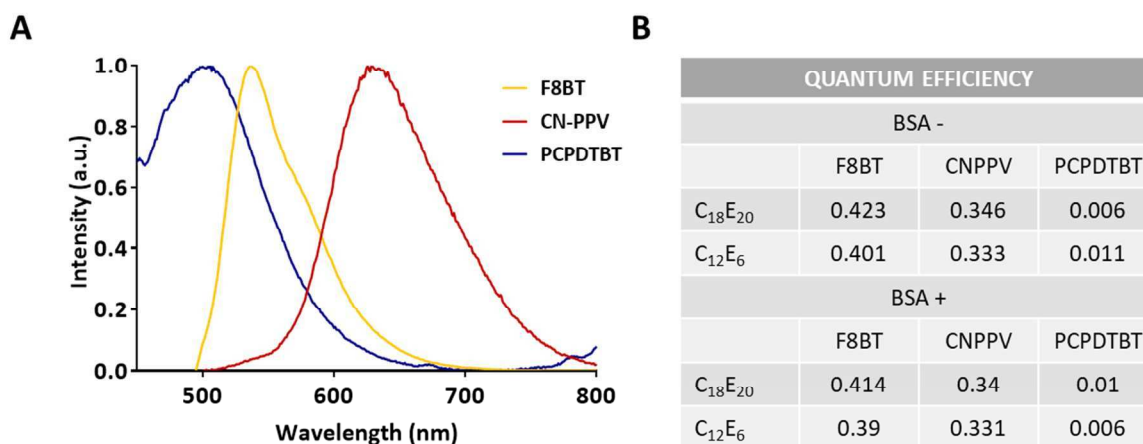

QUANTUM EFFICIENCY			
BSA -			
	F8BT	CNPPV	PCPDTBT
$C_{18}E_{20}$	0.423	0.346	0.006
$C_{12}E_6$	0.401	0.333	0.011
BSA +			
	F8BT	CNPPV	PCPDTBT
$C_{18}E_{20}$	0.414	0.34	0.01
$C_{12}E_6$	0.39	0.331	0.006

Figure 4. Normalized fluorescence spectra of F8BT CPNs, CN-PPV CPNs (a) and absolute quantum efficiency (b) of the conjugated polymer nanoparticle dispersions.

Effect of surfactant structure on protein binding

The introduction of CPNs into biological fluids containing proteins has been shown to lead to the displacement of the surfactant coating and the formation of a protein corona altering the CPN surface properties and quenching photoluminescence [46–48]. As stated previously, the consequence

of surfactant displacement from the CPN surface may be a loss in functionality, as well as an altered biodistribution or biocompatibility profile [49]. Thus, it is of interest to study the impact of conjugated polymer and surfactant chemistry on protein binding. In the current study, several complementary techniques were used to probe protein adsorption to CPNs, as well as the flat surface conjugated polymers. Two surfactants, $C_{12}E_6$ (HLB: 11.7) and $C_{18}E_{20}$ (HLB: 15.0), were selected for investigation in this phase of the study.

Hydrophobic interaction chromatography (HIC) and zeta potential measurements were used as indirect methods to investigate protein interactions with the CPN surface. HIC has been shown to be a versatile tool for the assessment of nanoparticle surface hydrophobicity, surfactant affinity to CPN surfaces and protein adsorption [14,15,28,40,50–52]. An HIC index score of 1.00 indicates a high nanoparticle surface hydrophobicity, as demonstrated by the HIC index score of polystyrene nanoparticles (0.96), which are used as a reference material [28,51]. HIC scores indicate that F8BT CPNs have a higher column material affinity (i.e. surface hydrophobicity) compared to CNPPV and PCPDTBT nanoparticles, regardless of the type of surfactant coating (Figure 5). Addition of BSA generally reduced interactions of the CPNs with the column material, indicating a possible adsorption of protein onto the particle surface. This hypothesis was substantiated by changes to the zeta potential of the nanoparticles following addition of BSA to the suspension. All CPN coated with $C_{12}E_6$ exhibited a significant increase in electronegativity following BSA addition indicating protein binding to the surface. In contrast, CPNs with a $C_{18}E_{20}$ coating did not exhibit changes in zeta potential.
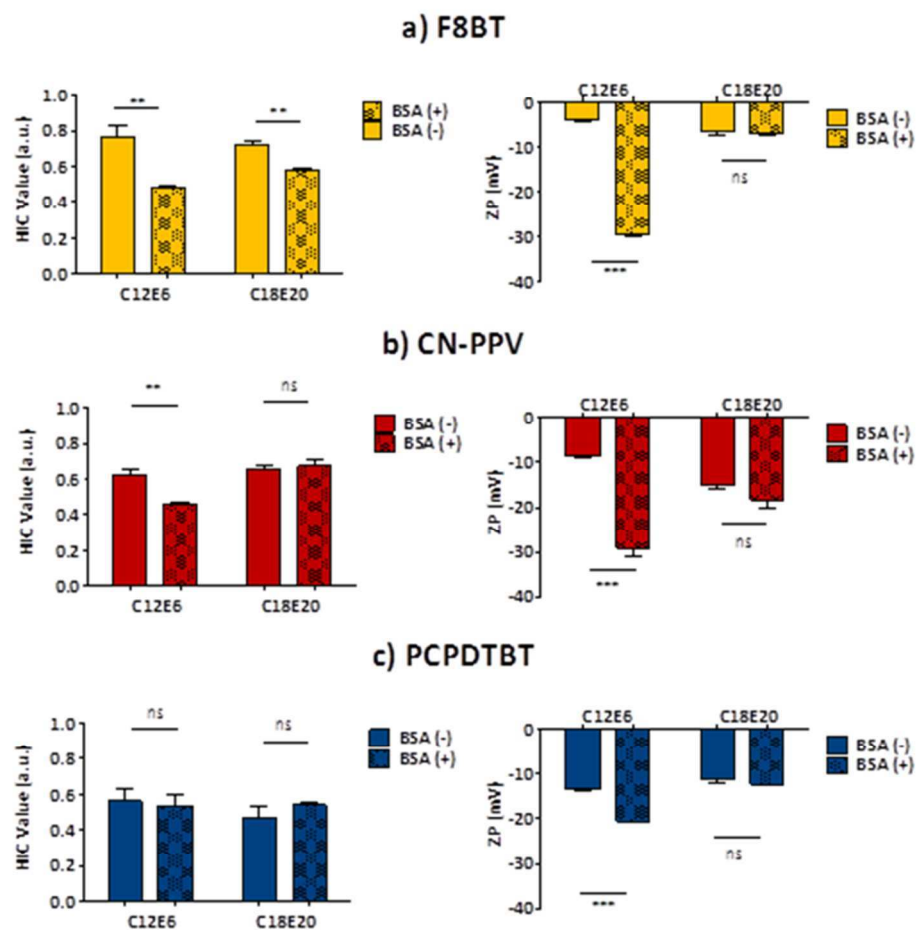
Figure 5. HIC index score (left panel) and zeta potential values (right panel) for A) F8BT, B) CN-PPV and C) PCPDTBT CPNs prepared with 1 mM $C_{12}E_6$ and $C_{18}E_{20}$, respectively. Prior to measurement, all systems were incubated 1 h at 37°C in either PBS or PBS supplemented with BSA (1 mg mL^{-1}), followed by a rigorous washing procedure to remove excess protein and surfactant. HIC index scores and zeta potential values represent the mean ± standard deviation of n=3 measurements. **p < 0.01, ***p < 0.001.

Contact angle analysis of uncoated F8BT, CN-PPV and PCPDTBT films revealed that the relative hydrophobicity of the conjugated polymers did not differ dramatically. Contrary to expectations, incubation with surfactant did not significantly improve the surface wettability,

except for the F8BT films, where $C_{18}E_{20}$ surfactant masked the hydrophobicity of the polymer film, improving its wettability by 10°. In contrast, subsequent incubation of the surfactant-coated films in a BSA solution significantly increased the film wettability in all cases. The differences between F8BT films coated with $C_{12}E_6$ vs. $C_{18}E_{20}$, were particularly pronounced, providing further evidence that $C_{18}E_{20}$ may present a more stable barrier to protein adsorption to F8BT compared to $C_{12}E_6$.
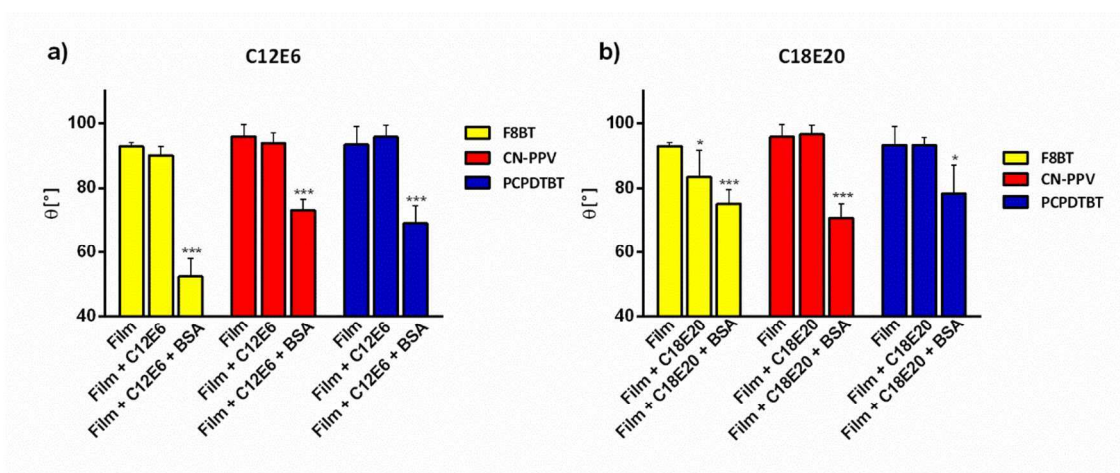

Figure 6. Contact angle measurements of conjugated polymer films (uncoated), following incubation with a surfactant solution (a: C12E6; b: C18E20) and subsequent incubation in a BSA solution. Values represent mean and standard deviations from n=6 measurements.

Quartz crystal microbalance with dissipation monitoring (QCM-D) is well suited for real-time monitoring of surfactant and protein adsorption at solid surfaces. Films exposed to $C_{12}E_6$ solutions (Figure 7, a-c) generally showed a rapid surfactant adsorption, followed by a significant mass loss during rinsing, indicative that the surfactant was washed off under flow. Injection of the BSA solution led to a minor mass increase in most cases, which was stable during a subsequent rinsing procedure, providing evidence of stable protein binding to the surface. The behaviour of $C_{18}E_{20}$ was more complex. In the case of F8BT surfaces (Figure 7d),

the surfactant showed a slow and continuous deposition onto the film, with only a fraction of the deposited mass removed during the rinsing step. The addition of BSA resulted in a rapid and significant mass loss, indicative of the protein removing surfactant from the polymer surface, possibly through solubilization, without a measurable mass increase due to protein adsorption. The addition of $C_{18}E_{20}$ to PCPDTBT films showed a similar behaviour, although surfactant adsorption to the surface occurred much more rapidly (Figure 7f). In contrast, the deposition of $C_{18}E_{20}$ onto CN-PPV films could not be characterized as the surfactant solubilised the film itself, thereby constantly removing mass from the system (Figure 7e).

Quantitative analysis of the QCM-D results to determine the adsorbed layer thickness[53] was challenging, because the analysis required the assumption of a coupled water content for each layer, which was difficult to account for in such a complex substrate. The system would need to be described as the combination of laterally homogeneous (conjugated polymer film) and heterogeneous films (surfactant/solvent layer and surfactant/solvent/BSA layer), therefore the quantitative interpretation of QCM data alone is severely limited[54]. For such reasons we chose not to include a film thickness determination in this study. In the future, additional information might be obtained by the combination of QCM with a method that can determine the mass of the adsorbate per surface area[55,56].
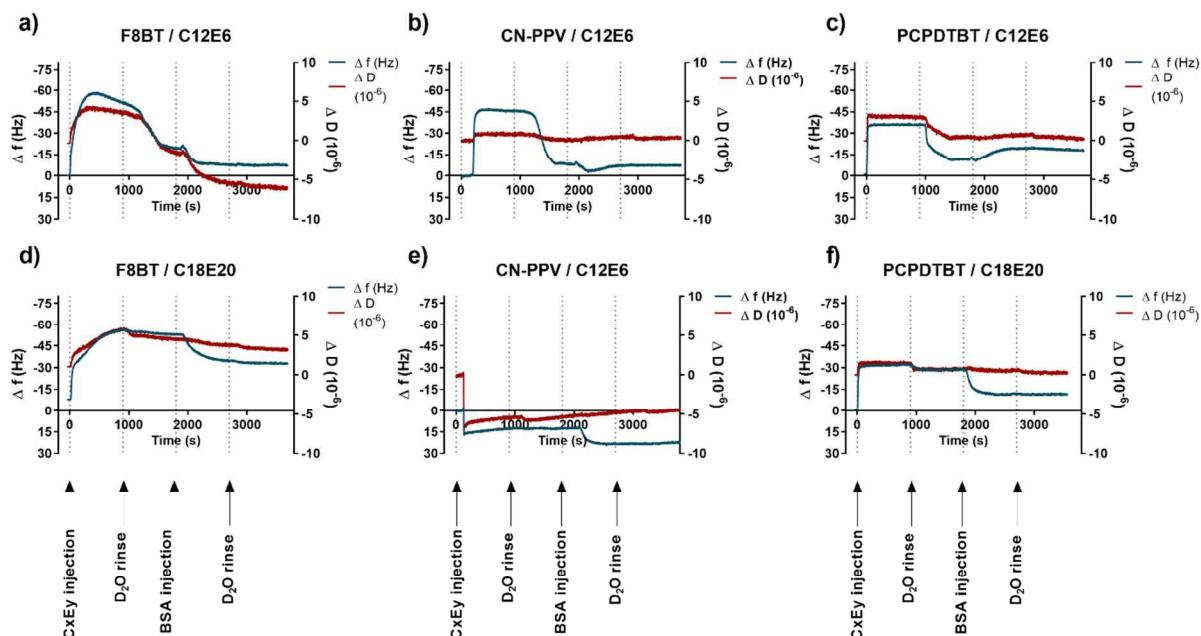
Figure 7. Frequency and dissipation shift versus time at the 3rd overtone. Conjugated polymer films were flushed for 10 min with either 1 mM $dC_{12}E_6$ (a-c) or $dC_{18}E_{20}$ (d-f) followed by a 5 min rest phase. Films were subsequently rinsed with D_2O followed by a flush with BSA solution and a further rinse phase. Experiments were performed in triplicate with representative traces chosen for the figure.

As a final complementary technique, neutron reflectometry (NR) was used to examine the potential protective effects of $C_{12}E_6$ and $C_{18}E_{20}$ coating against BSA adsorption to F8BT and PCPDBTB films, which were spin-coated onto silicon substrates. The success of these experiments was highly dependent upon the thickness of the polymer layer achieved by the spin-coating technique, and in this regard F8BT formed the most consistent samples in terms of uniform thickness and roughness (Table 4). The less uniform, highly rough PCPDTBT films produced by spin-coating significantly affected the accuracy of the mathematical fitting of the reflectivity curves (Supporting Information, Table S2 and Figure S4). Nevertheless, combined with the data obtained from the other surface analysis techniques, some pertinent conclusions

could still be drawn from the PCPDTBT results (see Supplementary Information). To improve the resolution of the NR data and thus the accuracy of the fitting, each experimental treatment was measured in at least three different solvent contrasts, the results from which were fitted simultaneously (See Supplementary Information Figures S1 to S3 for the full set of NR curves and fits for each sample in the different contrasts).

In order to fit the NR data, the samples were modelled as layers stacked upon the silicon substrate; a thin layer of silicon oxide on the substrate surface, the spin-coated conjugated polymer film, the hydrophobic tails of any surfactant adsorbed to the polymer, their hydrophilic head groups, and any adsorbed BSA contiguous with the bulk solvent. The simultaneous altering of the thickness, roughness, scattering length density (SLD; analogous to a neutron refractive index of the layer) and solvation of all these model layers, within physically reasonable limits, allowed theoretical NR curves to be fitted to the experimentally-obtained ones. An overall Chi-squared value obtained from the fitting software, together with the results of a bootstrapping error analysis on the parameter values obtained for each layer (run 100 times with 1000 iterations per run), were used to assess the closeness of the fits. In addition to obtaining theoretical NR curves, fitting also allowed the construction of SLD profiles for each experimental treatment, allowing the relationship between the thickness, solvation and roughness of each layer in the model to be represented graphically. For the purposes of making clear comparisons between the results of the various treatments, only the data obtained using D_2O and H_2O as bulk solvents are presented here (Figure 8), since these were deemed to show the highest degree of contrast between the different components of the samples.

For F8BT, exposure to BSA in the absence of a surfactant coating results in the formation of a clearly defined adsorbed protein layer (Figure 8A) with a fitted thickness of ~25 Å (Table 4).

The apparently high solvation of the BSA layer (80%) implies that coverage is fairly sparse, and taking this into account, the average thickness of the layer is consistent with that of BSA adsorbing to and flattening out on the surface of the hydrophobic polymer film[57].

The changes in the SLD profile observed upon addition of $d_{25}C_{12}E_6$ to uncoated F8BT (Figure 8B), clearly indicates that the surfactant adsorbs to the surface of the polymer. The accompanying decrease in F8BT hydration from 23% to 3 % (Table 4) suggests that the surface of the polymer may have been pitted or contained small cracks, which were filled by the adsorbing surfactant, thus displacing the solvent. This situation is the likely cause of the small peak in the H_2O contrast SLD profile which corresponds to the position of the surfactant chains, whereas a more discrete layer of surfactant would have resulted in a broader peak (such as that observed in Figure 8C). Overlap or intermixing between the alkyl chains and the PEG head group of the surfactant molecules are thus the likely reason for the narrow chains peak. When the $d_{25}C_{12}E_6$-coated F8BT sample was challenged with BSA, the SLD profile indicates a significant ingress of protein into the surfactant layers (seen most clearly from the H_2O contrast), which would be consistent with surfactant displacement and adsorption of the protein to the polymer, as was observed in both the contact angle and QCM-D experiments.

The addition of $C_{18}E_{20}$ to an F8BT film resulted in a discrete layer of surfactant adsorbing to the polymer surface, with little evidence of solvent displacement from surface irregularities (Table 4). The alkyl chain region of the surfactant is clearly visible in the SLD profiles (Figure 8C), suggesting very little overlap between the layers as indicated by the broad peak (H_2O contrast) or trough (D_2O contrast) showing the position of the hydrogenated C_{18} chains. The negligible solvation of the surfactant chains region (Table 4) suggests that these form an almost complete coating of the polymer surface, what might be thought of as a waxy layer. The SLD

profiles of the sample (Figure 8C) are substantially affected by the adsorption of BSA, which

must therefore act to displace the surfactant to some degree. The absence of a discrete peak

attributable to the protein, as was observed for both BSA absorbed directly to F8BT and in the

sample containing $d_{25}C_{12}E_6$, implies that comparatively less protein adsorbs to the surface in the

presence of $C_{18}E_{20}$. However, the large alteration in the SLD of the identifiable chain region

suggests that a significant amount of surfactant was removed from the polymer surface by the

protein. This is also highly consistent with the findings from contact angle and QCM-D
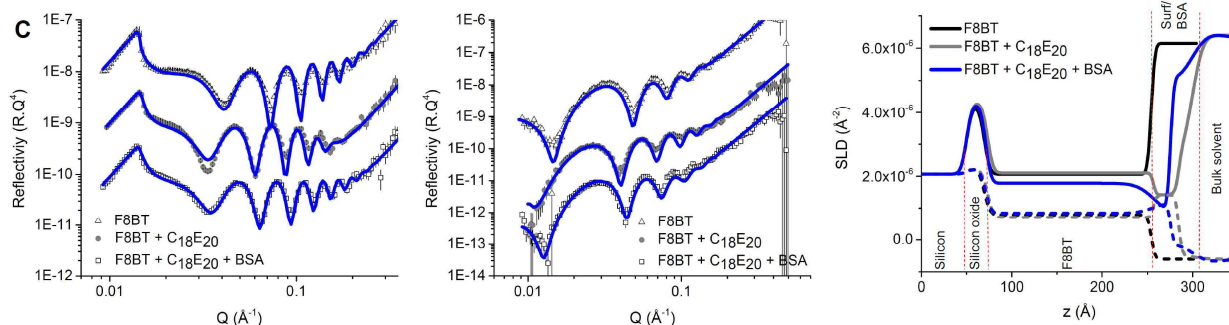
measurements.
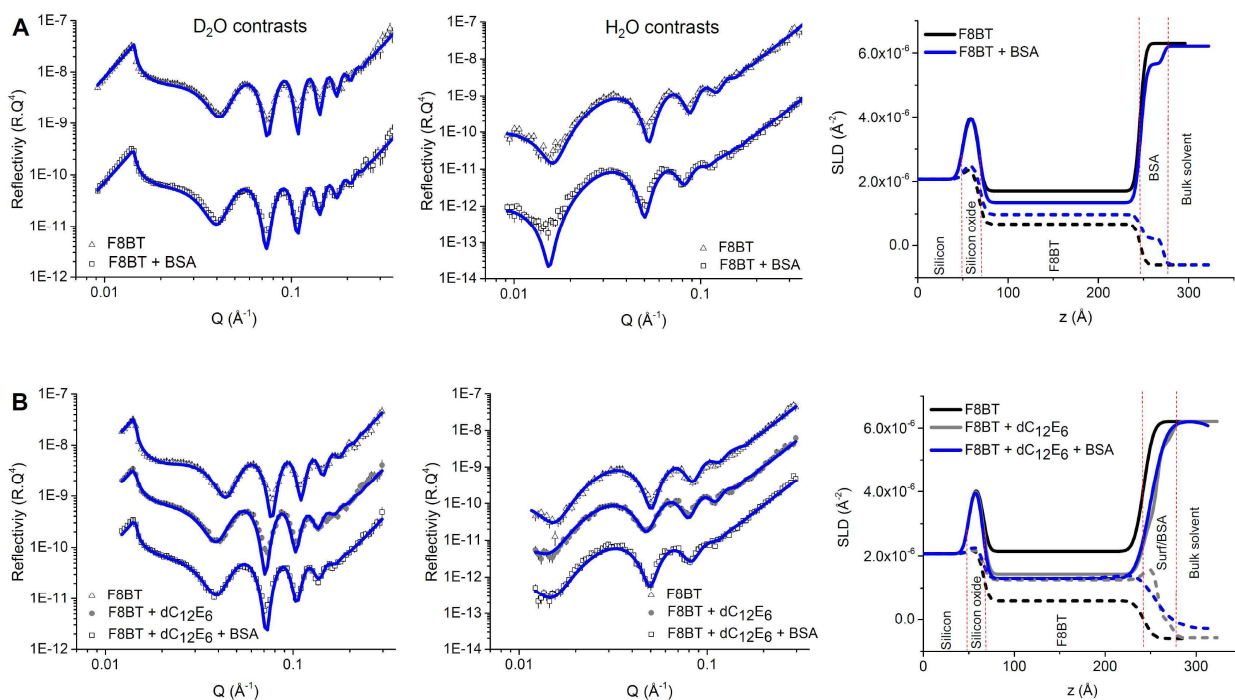
Figure 8. Experimentally obtained neutron reflectivity curves (data points) and their theoretical fits (blue curves) obtained in D_2O (left) and H_2O (centre) solvent contrasts, and their corresponding derived (right) SLD profiles (solid lines denote the D_2O contrast and dashed lines denote the H_2O contrast), comparing the sequential adsorption of surfactant and BSA onto F8BT-coated silicon substrates. (A) Shows the adsorption of BSA alone onto F8BT. (B) Shows the adsorption of $d_{25}C_{12}E_6$ to F8BT, followed by the adsorption of BSA and (C) shows the adsorption of $C_{18}E_{20}$ to F8BT, followed by the adsorption of BSA.

Table 4. Parameters obtained from the fitted neutron reflectivity for three different silicon substrates spin-coated with F8BT. The first column shows the effect of adsorption of BSA alone. The second column shows the effect of the sequential absorption of $d_{25}C_{12}E_6$ surfactant, followed by BSA. The third showing the effect of the sequential absorption of $C_{18}E_{20}$ surfactant, followed by BSA. The error values quoted for each of the parameters were determined by applying the Bootstrapping error analysis function interpolated within the RasCal data analysis software (run 100 times with 1000 iterations per run).

Fitted Parameters	F8BT	F8BT + BSA	F8BT	F8BT + $d_{25}C_{12}E_6$	F8BT + $d_{25}C_{12}E_6$ + BSA	F8BT	F8BT + $C_{18}E_{20}$	F8BT + $C_{18}E_{20}$ + BSA
Polymer thickness (Å)	179 ± 1	178 ± 2	177 ± 2	177 ± 8	177 ± 5	185 ± 2	183 ± 5	185 ± 6
Polymer SLD ($\times 10^{-6}$ Å^{-2})	0.90 ± 0.03	1.07 ± 0.05	0.93 ± 0.05	1.31 ± 0	1.31 ± 0	1.11 ± 0.19	1.03 ± 0.13	1.06 ± 0.06
Polymer roughness (Å)	5 ± 2	5 ± 3	8 ± 1	7 ± 3	10 ± 6	3 ± 3	3 ± 3	15 ± 1

Polymer hydration (%)	15 ± 3	6 ± 3	23 ± 2	3 ± 2	0 ± 0	19 ± 4	20 ± 0	14 ± 6
Surfactant tails thickness (Å)				15 ± 0	15 ± 0		28 ± 3	15 ± 0
Surfactant tails SLD (× 10^{-6} Å^{-2})				2.42 ± 0.29	1.47 ± 1.00		1.42 ± 0.25	1.07 ± 0.21
Surfactant tails roughness (Å)				4 ± 1	13 ± 1		3 ± 2	3 ± 5
Surfactant tails hydration (%)				25 ± 0	3 ± 11		0 ± 0	0 ± 2
Surfactant heads thickness (Å)				16 ± 2	8 ± 3		15 ± 4	19 ± 5
Surfactant heads SLD (× 10^{-6} Å^{-2})				2.49 ± 0.90	4.59 ± 1.16		-0.36 ± 0.26	0.94 ± 0.79
Surfactant heads roughness (Å)				5 ± 0	30 ± 1		10 ± 7	27 ± 5
Surfactant heads hydration (%)				80 ± 4	90 ± 5		42 ± 6	81 ± 10
BSA thickness (Å)		25 ± 0			5 ± 0			4 ± 1
BSA SLD (× 10^{-6} Å^{-2})		3.47 ± 0.53			5.23 ± 0.95			1.57 ± 0.77
BSA roughness (Å)		3 ± 0			23 ± 3			15 ± 0
BSA hydration (%)		80 ± 2			53 ± 7			45 ± 0
Chi squared of fit	18.9	24.8	14.2	16.1	17.6	17.4	45.3	16.9

Nanoparticle curvature is known to have a substantial effect on surfactant adsorption and packing density[58], as well as on the conformation of adsorbed proteins/peptides[59]. For example, surfactant packing density decreases on surfaces with a strong curvature and peptides show an increased tendency lose their secondary structure on nanoparticles smaller than 20 nm[59]. Heinz et al (2017) state that, as a general rule, flat surfaces may be a valid model for nanoparticles with a weak curvature, if the particle diameter is at least 20-fold greater than the length of the surfactant in its extended conformation[58]. NR data generated an estimated length of $C_{12}E_6$ as ~3.1 nm, which is close to literature values for similar surfactant structures[58] and may be a reasonable reflection of the extended conformation. This would indicate that the data generated with films (i.e. contact angle, QCM-D and NR measurements) represent a reasonable model for nanoparticles with a conjugated polymer core larger than 60 nm. NR estimates of the $C_{18}E_{20}$ length (4.3 nm) are most likely not indicative of the extended conformation, as the calculated

head group length (15 Å) is likely an underestimation due to coiling of the PEG chain in the solvent. Therefore, it may be reasonable to assume the $C_{18}E_{20}$ results from film-based experiments may marginally overestimate the packing density for any nanoparticles ~20-70 nm generated with the nanoprecipitation method.

Conclusions

This study contributes to the understanding of the structure and interactions at the interface of core-shell CPNs, essential to the design of clinically relevant diagnostic and therapeutic agents. A series of five non-ionic polyethylene glycol alkyl ether surfactants with varying HLB values were used as model surfactants to produce CPNs from three representative π-conjugated polymers: F8BT, CN-PPV and PCPDTBT. Contrary to the study hypothesis, the surfactant hydrophilic:lipophilic ratio did not influence CPN size or yield, which was dependent on the conjugated polymer properties. Surfactants with a longer alkyl chain ($C_{18}> C_{12}$) showed a higher affinity to F8BT and PCPDTBT surfaces and were less likely to be displaced from the polymer surface under simple flow conditions. Despite its higher surface affinity, $C_{18}E_{20}$ was also actively removed from the polymer surface in the presence of the serum protein, albumin. *In vivo*, this could result in a loss of CPN functionality or altered biocompatibility/biodistribution. It should be noted that the results of this study do not exclude the use of all amphiphilic molecules as coating agents for CPN production, but do encourage caution in the choice of stabilizing agents, especially if they are modified with a targeting agent.

The data from this study highlight the advantages of alternative CPN structures, such as crosslinking[60,61] or encapsulation[62–64]. Our group is currently exploring structures whereby the conjugated polymer is embedded within a matrix material (PEOlated di- and tri-block

copolymers with high molecular weight), thereby providing a better means of controlling CPN

properties and surface chemistry independent of the conjugated polymer properties[10,65,66].

Supporting Information. Urbano et al, 2018 (PDF)

AUTHOR INFORMATION

Corresponding Author

*Lea Ann Dailey

E-mail: lea.dailey@pharmazie.uni-halle.de

Present Addresses

[a] School of Cancer & Pharmaceutical Sciences, King's College London, 150 Stamford Street,

London SE1 9NH, UK

[b] Department of Bioengineering and Therapeutic Sciences, University of California, San

Francisco, California 94158, United States

[c] ISIS Spallation Neutron Source, Rutherford Appleton Laboratory, Harwell Science and

Innovation Campus, Didcot, Oxfordshire OX11 0QX, United Kingdom

[d]School of Physical Sciences, University of Kent, Canterbury, Kent, CT2 7NH, UK

[e] King's College London, Department of Physics, Strand Campus, London, UK

[g] Department of Chemistry, Imperial College London, London, U.K.

ᶠInstitut für Pharmazeutische Technologie und Biopharmazie, Martin-Luther-Universität Halle-Wittenberg, Halle, Germany. E-mail: lea.dailey@pharmazie.uni-halle.de

Funding Sources

REFERENCES

1.   Feng, X. *et al.* Conjugated polymer nanoparticles for drug delivery and imaging. *ACS Appl. Mater. Interfaces* **2,** 2429–35 (2010).

2.   Saranya, S. & Radha, K. V. Review of Nanobiopolymers for Controlled Drug Delivery. *Polym. Plast. Technol. Eng.* **53,** 1636–1646 (2014).

3.   Li, J., Rao, J. & Pu, K. Recent progress on semiconducting polymer nanoparticles for molecular imaging and cancer phototherapy. *Biomaterials* **155,** 217–235 (2018).

4.   Wu, C. & Chiu, D. T. Highly Fluorescent Semiconducting Polymer Dots for Biology and Medicine. *Angew. Chemie Int. Ed.* **52,** 3086–3109 (2013).

5.   Yu, J., Rong, Y., Kuo, C.-T., Zhou, X.-H. & Chiu, D. T. Recent Advances in the Development of Highly Luminescent Semiconducting Polymer Dots and Nanoparticles

for Biological Imaging and Medicine. *Anal. Chem.* **89,** 42–56 (2017).

6.   Braeken, Y., Cheruku, S., Ethirajan, A. & Maes, W. Conjugated Polymer Nanoparticles

for Bioimaging. *Materials (Basel).* **10,** 1420 (2017).

7.   Chen, H. *et al.* Highly absorbing multispectral near-infrared polymer nanoparticles from

one conjugated backbone for photoacoustic imaging and photothermal therapy.

Biomaterials **144,** 42–52 (2017).

8.   Vauthier, C. & Bouchemal, K. Methods for the Preparation and Manufacture of Polymeric

Nanoparticles. *Pharmaceutical Research* **26,** 1025–1058 (2009).

9.   Ahmad Khanbeigi, R. *et al.* Surface Chemistry of Photoluminescent F8BT Conjugated

Polymer Nanoparticles Determines Protein Corona Formation and Internalization by

Phagocytic Cells. *Biomacromolecules* **16,** 733–742 (2015).

10. Abelha, T. F. *et al.* Bright conjugated polymer nanoparticles containing a biodegradable

shell produced at high yields and with tuneable optical properties by a scalable

microfluidic device. *Nanoscale* **9,** 2009–2019 (2017).

11. Howes, P. *et al.* Magnetic conjugated polymer nanoparticles as bimodal imaging agents. *J.

Am. Chem. Soc.* **132,** 9833–9842 (2010).

12. Dai, R., Wu, F., Xu, H. & Chi, Y. Anodic, Cathodic, and Annihilation

Electrochemiluminescence Emissions from Hydrophilic Conjugated Polymer Dots in

Aqueous Medium. *ACS Appl. Mater. Interfaces* **7,** 15160–15167 (2015).

13. Behrendt, J. M. *et al.* Scalable synthesis of multicolour conjugated polymer nanoparticles

via Suzuki-Miyaura polymerisation in a miniemulsion and application in bioimaging. *React. Funct. Polym.* **107,** 69–77 (2016).

14.   Ahmad Khanbeigi, R. *et al.* Surface Chemistry of Photoluminescent F8BT Conjugated Polymer Nanoparticles Determines Protein Corona Formation and Internalization by Phagocytic Cells. *Biomacromolecules* **16,** 733–742 (2015).

15.   Khanbeigi, R. A. *et al.* Interactions of stealth conjugated polymer nanoparticles with human whole blood. *J. Mater. Chem. B* **3,** 2463–2471 (2015).

16.   Hashim, Z. *et al.* Gd-Containing Conjugated Polymer Nanoparticles: Bimodal nanoparticles for Fluorescence and MRI Imaging. *Nanoscale* **6,** 8376–8386 (2014).

17.   Fernando, L. P. *et al.* Mechanism of cellular uptake of highly fluorescent conjugated polymer nanoparticles. *Biomacromolecules* **11,** 2675–2682 (2010).

18.   Hashim, Z., Howes, P. & Green, M. Luminescent quantum-dot-sized conjugated polymer nanoparticles—nanoparticle formation in a miniemulsion system. *J. Mater. Chem.* **21,** 1797 (2011).

19.   Zhu, H. *et al.* Regulating Near-Infrared Photodynamic Properties of Semiconducting Polymer Nanotheranostics for Optimized Cancer Therapy. *ACS Nano* **11,** 8998–9009 (2017).

20.   Fessi H, Puisieux F, Devissaguet JP, A. N. Nanocapsule formation by interfacial polymer deposition following solvent displacement. *Int J Pharm* **55,** 1–4 (1989).

21.   Liu, Y. *et al.* Understanding the Robust Physisorption between Bovine Serum Albumin

and Amphiphilic Polymer Coated Nanoparticles. *ACS Appl. Mater. Interfaces* **8,** 2478–85 (2016).

22.   Ojha, B. & Das, G. Role of hydrophobic and polar interactions for BSA-amphiphile composites. *Chem. Phys. Lipids* **164,** 144–50 (2011).

23.   Ruso, J. M., Taboada, P., Varela, L. M., Attwood, D. & Mosquera, V. Adsorption of an amphiphilic penicillin onto human serum albumin: characterisation of the complex. *Biophys. Chem.* **92,** 141–53 (2001).

24.   Kim, J. & Somorjai, G. A. Molecular packing of lysozyme, fibrinogen, and bovine serum albumin on hydrophilic and hydrophobic surfaces studied by infrared-visible sum frequency generation and fluorescence microscopy. *J. Am. Chem. Soc.* **125,** 3150–8 (2003).

25.   Zunszain, P. A., Ghuman, J., Komatsu, T., Tsuchida, E. & Curry, S. Crystal structural analysis of human serum albumin complexed with hemin and fatty acid. *BMC Struct. Biol.* **3,** 6 (2003).

26.   Chidambaram, M. & Krishnasamy, K. Modifications to the conventional nanoprecipitation technique: an approach to fabricate narrow sized polymeric nanoparticles. *Adv. Pharm. Bull.* **4,** 205–8 (2014).

27.   McNaught, A. D. & Wilkinson, A. *Compendium of Chemical Terminology: IUPAC Recommendations*. (Blackwell Science, 1997).

28.   Jones, M. C. *et al.* Quantitative assessment of nanoparticle surface hydrophobicity and its

influence on pulmonary biocompatibility. *J. Control. Release* **183,** 94–104 (2014).

29.   Irache, J., Durrer, C., Ponchel, G. & Duchêne, D. Determination of particle concentration in latexes by turbidimetry. *Int. J. Pharm.* **90,** R9–R12 (1993).

30.   Stalder, A. F., Kulik, G., Sage, D., Barbieri, L. & Hoffmann, P. A snake-based approach to accurate determination of both contact points and contact angles. *Colloids Surfaces A Physicochem. Eng. Asp.* **286,** 92–103 (2006).

31.   Rodahl, M., Höök, F., Krozer, A., Brzezinski, P. & Kasemo, B. Quartz crystal microbalance setup for frequency and Q-factor measurements in gaseous and liquid environments. *Rev. Sci. Instrum.* **66,** 3924 (1995).

32.   Webster, J., Holt, S. & Dalgliesh, R. INTER the chemical interfaces reflectometer on target station 2 at ISIS. *Phys. B Condens. Matter* **385–386,** 1164–1166 (2006).

33.   Born, M. & Wolf, E. *Principles of Optics*. (Pergamon Press, Oxford, 1970).

34.   Huang, W. & Zhang, C. Tuning the Size of Poly(lactic-co-glycolic Acid) (PLGA) Nanoparticles Fabricated by Nanoprecipitation. *Biotechnol. J.* **13,** 1700203 (2018).

35.   Dovgolevsky, E. *et al.* Self-assembled conjugated polymer–surfactant–silica mesostructures and their integration into light-emitting diodes. *J. Mater. Chem.* **18,** 423–436 (2008).

36.   Zhang, C. *et al.* Understanding the correlation and balance between the miscibility and optoelectronic properties of polymer–fullerene solar cells. *J. Mater. Chem. A* **5,** 17570–17579 (2017).

37.   Dhoot, a. S. & Greenham, N. C. Triplet Formation In Polyfluorene Devices. *Adv. Mater.*
       14, 1834–1837 (2002).

38.   Zhan, X. & Zhu, D. Conjugated polymers for high-efficiency organic photovoltaics.
       Polym. Chem. **1,** 409 (2010).

39.   Theander, M. *et al.* High luminescence from a substituted polythiophene in a solvent with
       low solubility. *Chem. Phys. Lett.* **337,** 277–283 (2001).

40.   Tobío, M., Gref, R., Sánchez, A. et al. Stealth PLA-PEG Nanoparticles as Protein Carriers
       for Nasal Administration. *Pharm. Res.* **15,** 270–275 (1998).

41.   Peters, M. *et al.* PPV-Based Conjugated Polymer Nanoparticles as a Versatile Bioimaging
       Probe: A Closer Look at the Inherent Optical Properties and Nanoparticle–Cell
       Interactions. *Biomacromolecules* **17,** 2562–2571 (2016).

42.   Gettinger, C. L., Heeger, a. J., Drake, J. M. & Pine, D. J. A photoluminescence study of
       poly(phenylene vinylene) derivatives: The effect of intrinsic persistence length. *J. Chem.*
       Phys. **101,** 1673 (1994).

43.   Mitschke, U. & Bäuerle, P. The electroluminescence of organic materials. *J. Mater. Chem.*
       10, 1471–1507 (2000).

44.   Schwartz, B. J. CONJUGATED POLYMERS AS MOLECULAR MATERIALS : How
       Chain Conformation and Film Morphology Influence Energy Transfer and Interchain
       Interactions. *Annu. Rev. Phys. Chem.* **54,** 141–172 (2003).

45.   Pu, K. *et al.* Semiconducting polymer nanoparticles as photoacoustic molecular imaging

probes in living mice. *Nat. Nanotechnol.* **9,** 233–239 (2014).

46.   Sudeep, P. K. & Emrick, T. Functional Si and CdSe quantum dots: synthesis, conjugate

formation, and photoluminescence quenching by surface interactions. *ACS Nano* **3,** 4105–

9 (2009).

47.   Tetin, S. *Fluorescence Fluctuation Spectroscopy (FFS), pt. 2*. (Elsevier Science, 2012).

48.   Wolfram, J. *et al.* The nano-plasma interface: Implications of the protein corona. *Colloids

Surfaces B Biointerfaces* **124,** 17–24 (2014).

49.   Xia, X.-R., Monteiro-Riviere, N. a & Riviere, J. E. An index for characterization of

nanomaterials in biological systems. *Nat. Nanotechnol.* **5,** 671–675 (2010).

50.   Carstensen, H., Müller, B. W. & Müller, R. H. Adsorption of ethoxylated surfactants on

nanoparticles. I. Characterization by hydrophobic interaction chromatography. *Int. J.

Pharm.* **67,** 29–37 (1991).

51.   Staufenbiel, S. *et al.* Surface characterization and protein interaction of a series of model

poly[acrylonitrile-co-(N-vinyl pyrrolidone)] nanocarriers for drug targeting. *Int. J. Pharm.*

485, 87–96 (2015).

52.   Beck-Broichsitter, M., Bohr, A. & Ruge, C. A. Poloxamer-Decorated Polymer

Nanoparticles for Lung Surfactant Compatibility. *Mol. Pharm.* **14,** 3464–3472 (2017).

53.   Jin, J., Jiang, W., Yin, J., Ji, X. & Stagnaro, P. Plasma proteins adsorption mechanism on

polyethylene-grafted poly(ethylene glycol) surface by quartz crystal microbalance with

dissipation. *Langmuir* **29,** 6624–33 (2013).

54.   Reviakine, I., Johannsmann, D. & Richter, R. P. Hearing what you cannot see and visualizing what you hear: interpreting quartz crystal microbalance data from solvated interfaces. *Anal. Chem.* **83,** 8838–48 (2011).

55.   Bingen, P., Wang, G., Steinmetz, N. F., Rodahl, M. & Richter, R. P. Solvation effects in the quartz crystal microbalance with dissipation monitoring response to biomolecular adsorption. A phenomenological approach. *Anal. Chem.* **80,** 8880–90 (2008).

56.   Johannsmann, D., Reviakine, I., Rojas, E. & Gallego, M. Effect of sample heterogeneity on the interpretation of QCM(-D) data: comparison of combined quartz crystal microbalance/atomic force microscopy measurements with finite element method modeling. *Anal. Chem.* **80,** 8891–9 (2008).

57.   Cowsill, B. J. *et al.* Measurement of the thickness of ultra-thin adsorbed globular protein layers with dual-polarisation interferometry: a comparison with neutron reflectivity. *Soft Matter* **7,** 7223 (2011).

58.   Heinz, H. *et al.* Nanoparticle decoration with surfactants: Molecular interactions, assembly, and applications. *Surface Science Reports* **72,** 1–58 (2017).

59.   Mandal, H. S. & Kraat, H. B. Effect of the surface curvature on the secondary structure of peptides adsorbed on nanoparticles. *J. Am. Chem. Soc.* **129,** 6356–6357 (2007).

60.   Yu, J. *et al.* Stable Functionalization of Small Semiconducting Polymer Dots via Covalent Cross-Linking and Their Application for Specific Cellular Imaging. *Adv. Mater.* **24,** 3498–3504 (2012).

61. Zhou, L., Geng, J., Wang, G., Liu, J. & Liu, B. Facile Synthesis of Stable and Water-Dispersible Multihydroxy Conjugated Polymer Nanoparticles with Tunable Size by Dendritic Cross-Linking. *ACS Macro Lett.* **1,** 927–932 (2012).

62. Joshi, P. B. & Zhang, P. Facile capture of conjugated polymer nanodots in silica nanoparticles to facilitate surface modification. *J. Mater. Sci.* **50,** 3597–3603 (2015).

63. Changfeng Wu, Craig Szymanski, and & McNeill*, J. Preparation and Encapsulation of Highly Fluorescent Conjugated Polymer Nanoparticles. (2006). doi:10.1021/LA060188L

64. Geng, J., Liu, J., Liang, J., Shi, H. & Liu, B. A general approach to prepare conjugated polymer dot embedded silica nanoparticles with a SiO2@CP@SiO2 structure for targeted HER2-positive cellular imaging. *Nanoscale* **5,** 8593–601 (2013).

65. Abelha, T. F. *et al.* Bright conjugated polymer nanoparticles containing a biodegradable shell produced at high yields and with tuneable optical properties by a scalable microfluidic device. *Nanoscale* **9,** 2009–2019 (2017).

66. Crossley, D. L. *et al.* Post-polymerization C–H Borylation of Donor–Acceptor Materials Gives Highly Efficient Solid State Near-Infrared Emitters for Near-IR-OLEDs and Effective Biological Imaging. *ACS Appl. Mater. Interfaces* **9,** 28243–28249 (2017).

1
2
3
4
5
6
7
8
9
10
11
12
13
14
15
16
17
18
19
20
21
22
23
24
25
26
27
28
29
30
31
32
33
34
35
36
37
38
39
40
41
42
43
44
45
46
47
48
49
50
51
52
53
54
55
56
57
58
59
60

TOC graphic

Flow → C_xE_y surfactant

Flow → C_xE_y surfactant

Albumin

Conjugated polymer nanoparticle surface

Conjugated polymer nanoparticle surface